Report

Design of an ultrafast pulsed ponderomotive phase plate for cryo-electron tomography

Graphical abstract

Highlights

- Interactions between pulsed electrons and photons may enhance contrast in cryo-EM

- Theoretical design of a pulsed phase plate to achieve efficient phase contrast

- Simulate pulsed electron beam phase-shifted by 90° via timed picosecond laser pulse

- Continuous electron beams are too sporadic and stochastic to be used with pulsed laser

Authors

Daniel X. Du, Anthony W.P. Fitzpatrick

Correspondence

anthony.fitzpatrick@columbia.edu

In brief

Zernike phase plates are known to increase the contrast of soft matter in light microscopes. Analogous devices for electron microscopes are being designed to increase collection efficiency for short-lived specimens. Here, Du and Fitzpatrick describe a set of laser parameters that will produce the necessary phase shifts in pulsed electrons.
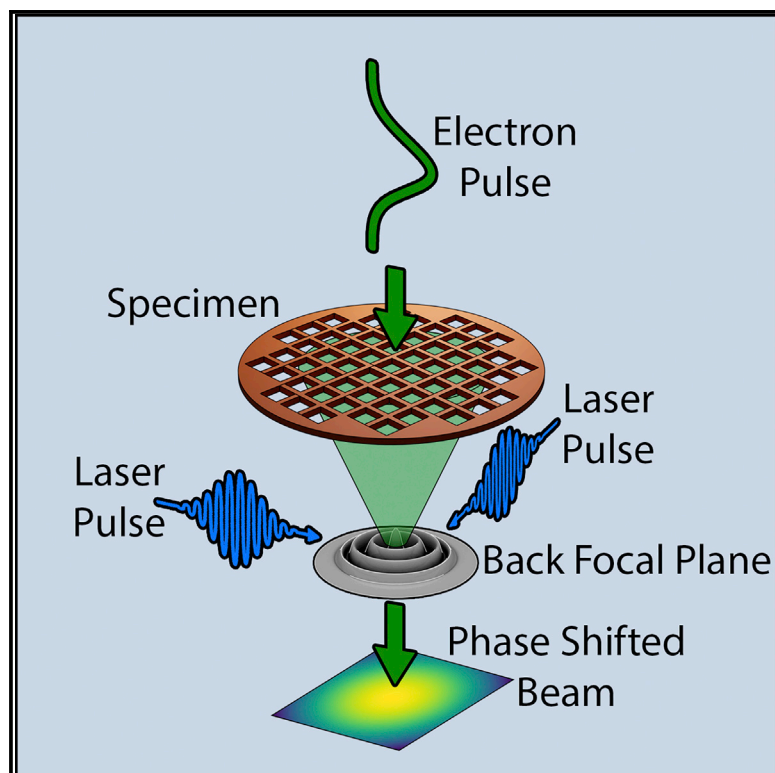
CellPress

Report

Design of an ultrafast pulsed ponderomotive phase plate for cryo-electron tomography

Daniel X. Du[1,2,3] and Anthony W.P. Fitzpatrick[1,2,3,4,*]

[1]Mortimer B. Zuckerman Mind Brain Behavior Institute, Columbia University, New York, NY 10027, USA
[2]Department of Biochemistry and Molecular Biophysics, Columbia University, New York, NY 10032, USA
[3]Taub Institute for Research on Alzheimer's Disease and the Aging Brain, Columbia University Irving Medical Center, 630 West 168th Street, New York, NY 10032, USA
[4]Lead contact
*Correspondence: anthony.fitzpatrick@columbia.edu
https://doi.org/10.1016/j.crmeth.2022.100387

MOTIVATION   While single-particle cryo-electron microscopy (cryo-EM) is routinely used to determine protein structure to a high resolution, cryo-electron tomography (cryo-ET) contends with crowded cellular environments and low individual protein copy numbers, making detection, identification, and in-cell structure determination challenging. A common hypothesis to remedy the low-contrast of cryo-ET is to use phase-interference microscopy with a phase plate, analogous to Zernike phase microscopy. Here, we outline the design of a pulsed ponderomotive phase plate as an alternative method to enhance phase contrast in cryo-EM. While continuous beam ponderomotive phase plates produce the high fluences necessary through resonators, we demonstrate that such high fluences are achievable *ex situ* through the condensed nature of pulsed laser beams and briefly explore various modalities in which a pulsed ponderomotive phase plate may operate.

SUMMARY

Ponderomotive phase plates have shown that temporally consistent phase contrast is possible within electron microscopes via high-fluence static laser modes resonating in Fabry-Perot cavities. Here, we explore using pulsed laser beams as an alternative method of generating high fluences. We find through forward-stepping finite element models that picosecond or shorter interactions are required for meaningful fluences and phase shifts, with higher pulse energies and smaller beam waists leading to predicted higher fluences. An additional model based on quasi-classical assumptions is used to discover the shape of the phase plate by incorporating the oscillatory nature of the electric field. From these results, we find the transient nature of the laser pulses removes the influence of Kapitza-Dirac diffraction patterns that appear in the static resonator cases. We conclude by predicting that a total laser pulse energy of 8.7 μJ is enough to induce the required $\pi/2$ phase shift for Zernike-like phase microscopy.

INTRODUCTION

The imaging of biological specimens, and soft matter in general, has significantly advanced to the point where high-resolution structure determination of protein complexes is becoming increasingly commonplace.[1–4] However, this process itself is not without its difficulties, both for single particle cryo-electron microscopy (cryo-EM) and cryo-electron tomography (cryo-ET). At resolutions better than 4 Å, required to identify side chains, tens of thousands of particles are acquired, aligned, and superimposed to produce sufficient contrast for structure determination.[5–9] In addition, numerous software-based contrast enhancement techniques must be applied to aid in segmentation and annotation of cryo-electron tomograms.[5,9–15] Much of the reason for the time

and effort invested in these forms of image processing can be attributed to the weak scattering of electrons from soft or low-atomic number (low-Z) matter.[16–18]

Indeed, this problem has originated in optical microscopy and was eventually mitigated either by an intentional defocusing of the objective to acquire phase-dependent fringes or through the development of the Zernike phase microscope. The Zernike phase microscope enhances phase contrast by altering the phase of the unscattered light transmitted from a specimen by a factor of $\pi/2$. This additional factor creates destructive interference, much like Bragg diffraction, and thus enhances contrast at feature boundaries.[19] This concept has long been theoretically extended to the electron microscope, but only recent advancements have made such phase shifts possible to an electron
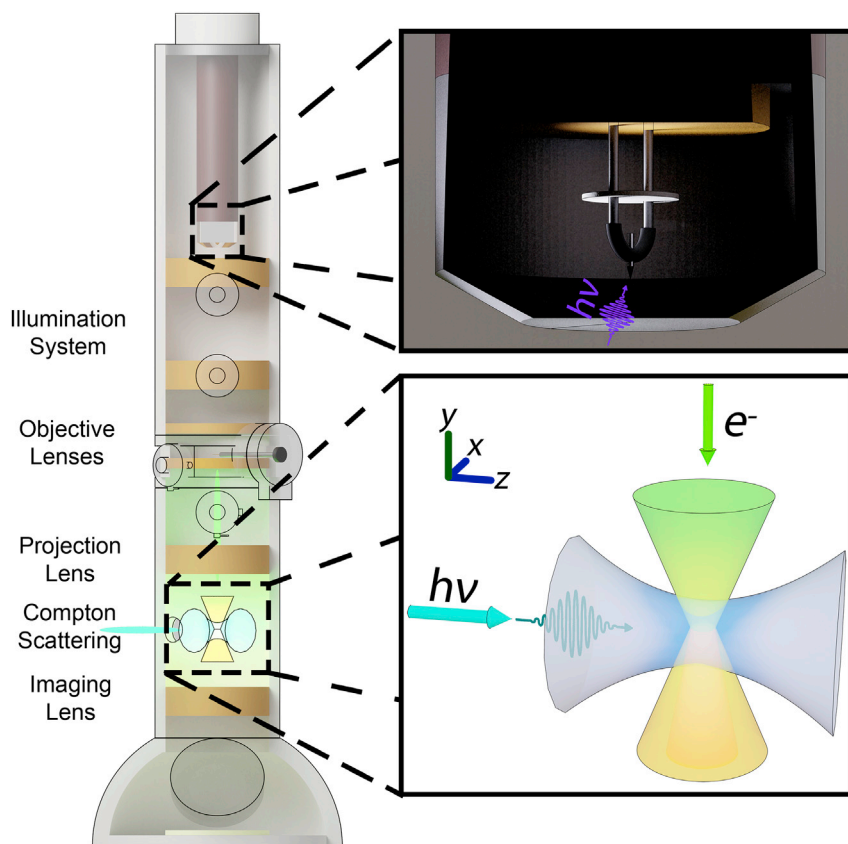
Figure 1. A cross-section of the pulsed ponderomotive phase plate operating inside an ultrafast electron microscope

Each of the major sections of the TEM, including the region with the ponderomotive phase plate, is labeled. Here, the region with Compton scattering is specifically targeted to a location where the back focal plane of the specimen is reformed, allowing for the scattering against the direct (000) peak. In the upper inset, a schematic demonstrates the generation of the pulsed electron beam with an UV laser pulse. In the bottom inset, a closeup of the ponderomotive phase plate demonstrates where the laser beam waist is positioned such that it has the highest density of photons for Compton scattering. Likewise, the electron beam experiences a refocusing of the back focal plane at the exact same location. Here, only the direct beam is shown.

beam.[20–24] Most prominently, the Volta phase plate and other such material-based phase plates have demonstrated sharp increases in contrast, although these methods still struggle with electrostatic charging and beam damage.[21,24–29]

An alternative to material phase plates proposed by Reed et al.[23,30] in a patent used a ponderomotive field potential generated by focused laser beams to alter the phase of electrons in a narrow field of view, with the aim of avoiding any deleterious effects such as material damage or charging. Recently, this idea has been implemented in two continuous wave forms with the inclusion of resonators to reach the required powers for sufficient Compton scattering. The first involves a Fabry-Perot resonator and the second uses a ring micro-resonator. Already, early results show similar contrast enhancements to material phase plates and work continues to mitigate the aberrations that occur from scattering and physically changing the column of the transmission electron microscope (TEM).[31–34]

The use of a continuous resonating beam enables the formation of a stable, continuously replenishing phase plate, thereby bypassing the charging and damage concerns of material phase plates. However, a resonator is not the only method to localize the power in a laser beam. As an alternative, pulsed beams, capable of being produced *ex situ*, are well known to achieve high instantaneous fluences.[35] Here, we explore the proposed pulsed ponderomotive phase plate, as demonstrated in Figure 1, and determine the various experimental parameters required for efficient phase contrast via a forward-stepping finite element model. It is our intent to understand if the sharp increase in fluence at the beam waist of an ultrafast laser is sufficient to generate the required $\pi/2$ phase shift relative to the unscattered electrons and to further explore the effects of changing electron and laser spatiotemporal pulse widths.

We discuss this form of the phase plate as a minimally invasive and flexible *ex situ* method of delivering similar phase shifts by compressing the laser beam in both space and time rather than force a large fluence to be present within the microscope column at every point in time. In fact, the amount of energy delivered to such small optical components may lead directly to warping and a loss in resonator coherence. Moreover, placing such optics in the column creates additional spherical and chromatic aberration as the beam has to be directed into and out of the center of the resonator cavity.[31] This is avoidable using a windowed ultrafast pulse system with guidable laser beams that can freely move the interaction region. Such pulsed techniques will not work for a conventional TEM unless incredibly high frequency lasers in the gigahertz range are developed. In an ultrafast electron microscope (UEM), this becomes possible by controlling when and where the electrons overlap with the photons. There are two models we will use to explore the interaction between electrons and photons: one resulting from a fundamental scattering frame and one from a quasi-classical frame, which have been adapted to fit a forward-stepping algorithm.[22,31] The two models are used for distinct purposes that are discussed later. The results of these investigations are aimed at guiding future development in the pulsed ponderomotive phase plate. The data presented here include temporal interactions that range from picoseconds to nanoseconds, a set of parameters matching the experimental envelope of already existing ultrafast TEM systems.[34,36,37] Moreover, the spatial interactions range from micrometers to millimeters, which reach the physical bounds of reasonable interactions within the limited space and accessibility of electron microscope columns. A recent report[38] discussing the use of radiofrequency
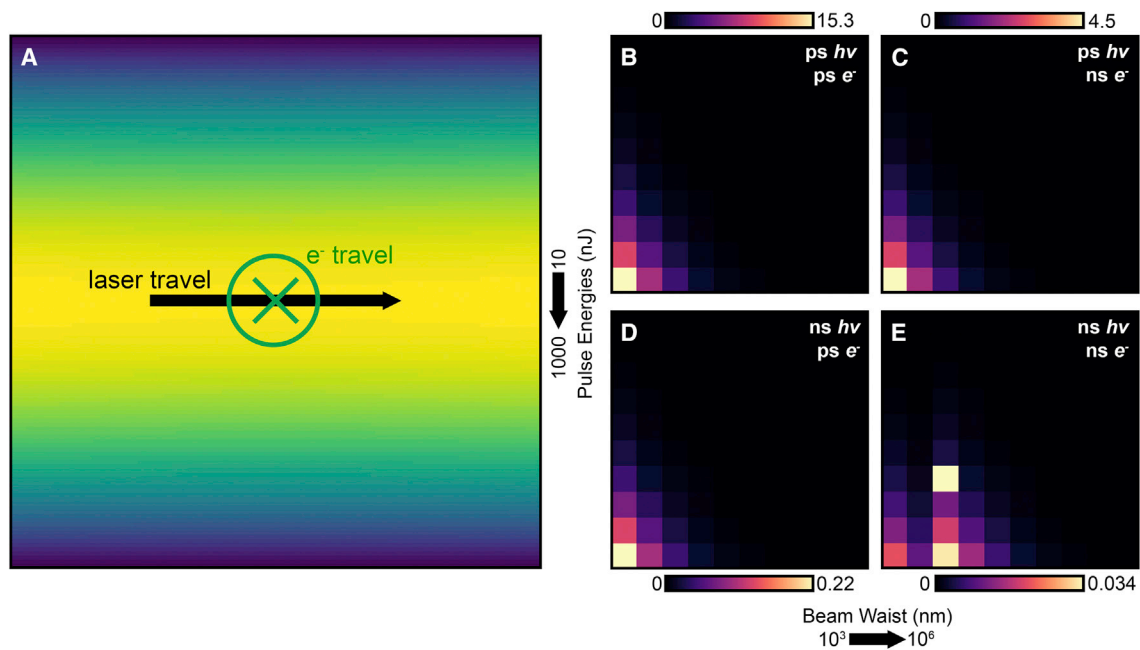
Figure 2. A demonstration of the simulated results alongside contour plots of the peak difference in phase shift between the point of maximum shift and the point of minimum shift

(A) A typical result from the simulations involving the scattering method, with the direction of laser travel progressing from left to right and the electron beam traveling into the page.

(B–E) Contour plots of the phase shift difference in the electron beam. The pulse energies are along the *y* axes, with values from 10 nJ to 1,000 nJ in logarithmic form. The *x* axes describe the beam waist size from 1 μm to 1 mm. Color bars have been included with each contour plot showing the phase shift, with each color bar normalized to the peak shift in the contour plot. The temporal resolutions (1σ) of both the laser and electron beams are shown in the top right.

cavity-generated electron pulses at high repetition rates ranging from 56 to 420 MHz showed that laser pulses operating at central wavelengths of 800 and 1,500 nm with pulse durations of 100 and 300 fs could reach the required phase shifts at much smaller spatial constraints than the ones discussed in this article. Importantly, the smaller beam waists presented in that report dramatically decreased the required pulse energy compared with the energies discussed here.

RESULTS

Initial experimental bounds with the scattering method

The most prominent aspect of the pulsed ponderomotive phase plate is determining whether a pulsed laser beam even has enough photon density to generate the required $\pi/2$ phase shift for Zernike phase contrast. Here, we use one of the theories set forth by Müller et al.[22] and described by a four-particle Feynman diagram. The phase shift from the ponderomotive effect is then generally described by the following equation:

$$\delta\varphi = \frac{\hbar\alpha\rho\lambda\delta t}{\left[m_e^2 + \frac{p^2}{c^2}\right]^{1/2}},$$

where α is the fine-structure constant, ρ is the instantaneous photon density in the presence of the scattered electron, λ is the wavelength of the photons, p is the momentum of the elec-

tron, and δt is the measured interaction time. Using this equation, we simulated the interaction between a photon pulse of 515 nm in wavelength and an electron pulse of 200 keV electrons. To keep the problem simple, the laser beams used in the simulation are of a TEM$_{00}$ Gaussian beam, adapted to fit an ultrafast temporal profile.[39] The equation used to approximate an ultrafast Gaussian pulse is described by:

$$I(\rho_{xy}, z, t) = \frac{A(t)}{\pi\omega^2(z)}\exp\left[-\frac{2\rho_{xy}^2}{\omega^2(z)}\right]f(t)$$

$$f(t) = \exp\left[-\frac{2(z-ct)^2}{\sigma_t^2 c^2}\right]$$

$$\omega^2(z) = \omega_0^2\left[1 + \frac{z^2}{z_0^2}\right],$$

where $A(t)$ is a time-varying parameter used to normalize the pulse to the pulse energy, $\omega(z)$ is the Gaussian beam diameter, z_0 is the Rayleigh range, ρ_{xy} is the radial distance from the travel axis of the laser, σ_t is the time resolution, c is the speed of light, and z is the distance down the travel axis. More on the implementation of this simulation is discussed in the STAR Methods section and in Figures S1, S2, and S3. The results of these simulations are summarized in Figure 2. An example contour is provided as well,

which describes the result of interactions from electrons traveling at different angles through the laser beam. For this simulation, each pixel of the contour represents an electron path of a different slope that all pass through the center of the laser beam (marked by the direction of electron travel) in a cone as the pulse center of the laser beam passes through the origin. As such, electrons represented by pixels on the right travel counter to the direction of the laser beam in the xz-plane. Electrons represented by pixels on the left travel in the same direction as the laser beam in the xz-plane. Electrons in pixels at the top travel toward $-x$, and those at the bottom travel toward $+x$. As is the case in electron microscopes, these electrons also all primarily travel in the $-y$ direction, which is orthogonal to the plane of the contour plot and extends into the face of the page.

The immediately noticeable result is the expected trend of higher beam powers generating a greater amount of phase shift, a result that arises directly from the interaction equation and the photon density term. Similarly, the photon density is increased when the beam waist narrows, another expected result from the Gaussian pulse equations. Aside from the obvious mathematical consequences to the phase shift resulting from the choice of model, the $\pi/2$ Zernike phase shift is exceeded in only two of the temporal resolution cases tested. Here, we have tested the model by varying the laser and electron pulses between 10 ps and 1 ns in pulse duration (i.e., standard deviation). Out to 1 μJ of pulse energy, the phase shift exceeds the $\pi/2$ requirement when the laser beam is condensed to 10 ps, as expected based on the resulting instantaneous photon densities. In the case of matching electron and laser pulse durations, the expected phase shift is 15.3 radians at the peak, while a mismatched nanosecond electron beam generates a 4.5-radian phase shift.

We note the odd behavior in the contour plots for the cases of nanosecond laser and electron pulses. This behavior is due to a lack in time granularity in electron slice stepping, which is unfortunately necessary to alleviate computational overhead. Without such overhead, we would expect a monotonic increase toward bottom left (i.e., smaller beam waist, higher pulse energy). Future simulations may account for this by incorporating non-uniform meshes, although it is not a primary concern; we are more interested in the trend, order-of-magnitude phase shifts, and shape of the pulsed phase plate.

It is important to further discuss the reporting of phase as an average phase difference across the entirety of an electron pulse. Here, we note that while the average phase increase in the case of a 10-ps laser pulse and 1-ns electron pulse reaches the adequate average phase shift necessary for phase contrast, a deeper exploration of the total number of electrons that shift in phase reveals the shift only exists in the pulse duration where both the laser and electrons overlap. As such, only a limited section of the electrons in this scenario shows any appreciable phase shift. From the results of these preliminary simulations, we focus attention on the most promising cases of short-duration 10-ps pulses for much of this article.

Single- and double-laser quasi-classical approximation for shape determination

The shape of the phase plate is of concern, as it has a direct effect on the contrast transfer function and analysis of the resulting

image.[40] It is well known that in the context of a continuous wave, the oscillatory nature of the photons form a Kapitza-Dirac diffraction grating, which is also imprinted onto the phase shifted electrons.[41] In the pulsed case, it is unclear if this diffraction grating would be as clearly resolved. We hypothesize the transient nature of both the electron and laser pulses would smear the original Kapitza-Dirac diffraction grating and would approach the results from the scattering model. The central equation governing the shape of the phase plate resulting from scattering against the oscillatory fields is given by the following:

$$\varphi = \int dt \cdot A_0^2 \left[1 - \beta^2 \cos^2 \left(\frac{2\pi z}{\lambda} \right) \cos^2 \theta \right]$$

$$A_0 = \frac{C_0}{\omega(z)} \exp \left[-\frac{\rho_{xy}^2}{\omega^2(z)} \right] f(t),$$

where C_0 is some arbitrary vector amplitude measured in volts, $\beta = v/c$, and θ is the polarization of the laser (here set to zero). This model has been adapted from Axelrod et al.[42] and Turnbaugh et al.[31] and once again changed to fit ultrafast pulse interactions. Because of the ambiguous nature of C_0 in the context of electric fields from photons, particularly in relation to its ultrafast behavior, we opt instead to use this method to determine the shape result instead of any given magnitude in phase shift. The results of this model, some of which are shown in Figure 3, highlight differences between varying laser powers and beam waists.

The smearing effect expected from the interacting traveling waves is shown clearly in Figure 3. At smaller laser beam waists, the phase shift matches the results from the fundamental scattering model. However, by moving to the far more realistically feasible beam waist of 1 mm, we observe a stronger phase shift in electrons traveling in the same direction to the laser beam, an expected result for electrons that spend additional time in the high-intensity regions of the laser beam. This smearing effect has been carefully checked by varying numerous simulation parameters. Nonetheless, we still do not observe any form of regular or repeating structure to the phase shift as expected from Kapitza-Dirac diffraction or as the mathematical form of the model suggests. Moreover, there is no change in the profile as the power increases, indicating that the smearing effect occurs regardless of the pulse energy.

One theory on mitigating the isotropic effects of a single laser has been to use two laser beams, positioned orthogonal to each other, such that the resulting phase shift forms rings or circles rather than lines.[41] Here, we explore this hypothesis using an extension of both models by simply adding another laser source of equivalent characteristics oriented perpendicularly (i.e., traveling in the x axis) to the original source and with the same polarization and power, as shown in Figure 3A. The addition of a second laser only circularizes the phase shift in certain scenarios where the shift originally extends completely along the travel direction. However, Figure 3C shows in cases where the beam size is large and the resulting phase shift is prominently skewed toward electrons traveling alongside the laser travel
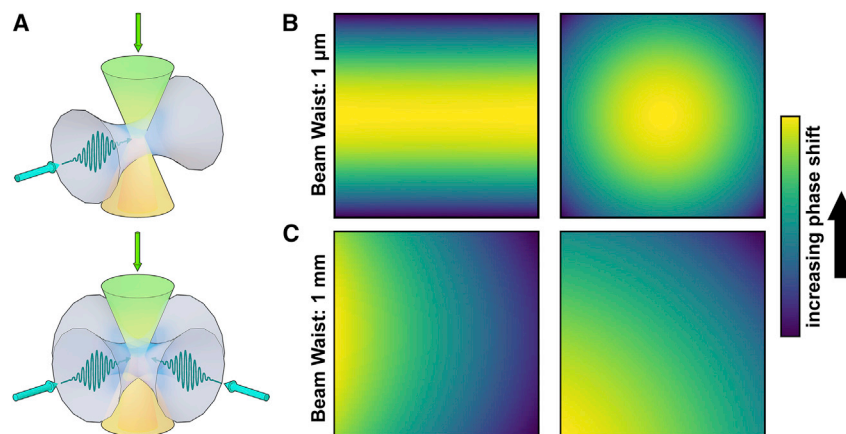
Figure 3. The contour plots displayed here are representative plots chosen from a wider range of tested experimental parameters and demonstrate the range of contours that appear from solving the quasi-classical model

Major variances in phase shift shape are a result of changes in beam waist size and no other simulated experimental parameters showed significant variations in the phase plate shape. A color bar has been included at the right to show darker regions of lower phase shift and brighter regions with higher phase shift.

(A) Schematic of one laser and two laser geometries in the ponderomotive phase plate with associated typical contour plots in the quasi-classical simulations.

(B) Corresponds with profiles with a laser beam waist size of 1 μm.

(C) Corresponds with solutions at laser beam waists of 1 mm.

direction, the expected circularization does not occur. In no cases does there seem to be a reappearance in Kapitza-Dirac diffraction. From these simulations, we can preliminarily conclude that such a grating only occurs in situations where the grating is static.

So far, these results have been discussed in the context of an electron beam that condenses to a singular or infinitesimally small point at the center of the laser beam (i.e., time zero). It is important to note that while this provides a basis for which to continue discussions on the feasibility of a pulsed ponderomotive phase plate, the amplitude of any such phase shifts will be artificially inflated, as all electrons pass through the most intense region of the laser beam. To address this, another layer of the model must be added to include the effects of a finite-sized electron beam crossover.

Size effects in both approximations and emission behavior

Of course, an infinitesimally small cross-over for the electron beam is an unreasonable expectation. In fact, in most electron microscopes, the direct beams are usually fit directly to a Gaussian or a Lorentzian as part of the instrument response function convoluted with the specimen response. We can take such a principle and apply it to the models provided above, where we perform simulations on pulsed beams passing through a region 200 μm across (a commonly available aperture size) and split into 30 sections, an arbitrary voxel size dictated by computational necessity, in both the x and z directions. Using a Gaussian with a similar width fit to 200 μm, each section is given a weight that is then used to calculate the average phase shift.

Figure 4 describes this addition to the calculation in more detail. Arrayed in the cross-over region are the numerous simulation points denoted by cones that converge to infinitesimally small points. To join these simulation points together, a weighted sum is taken of each congruent angular direction (i.e., each independent travel direction), which either combine in the far limit or are reassembled at the image by additional lenses. For the sake of computational efficiency, the number

of simulation points is diminished from the native granularity of each simulation. As such, each final point must include multiple "voxels" from the simulation matrices, as demonstrated in Figure 4A. Here, we simulate the effect of a 1-nJ laser pulse interacting with an electron pulse during the span of a single nanosecond. The interaction region for the laser is 100 μm in beam diameter at its waist.

By including the effects of size, we immediately observe a decrease in the expected phase shifts. This is an expected result; the effects of the ponderomotive force are spread out into a finite region rather than a singular point for each electron to pass through. Interestingly, both the fundamental scattering and quasi-classical models converge to the same shapes, regardless of the underlying interaction equations. Three separate beam waist and pulse energy conditions are tested: 100 nJ at 1 μm, 1 nJ at 100 μm, and 100 nJ at 100 μm. The resulting phase shifts for a single laser beam are, respectively, 0.50 radians, 1.8×10^{-4} radians, and 1.8×10^{-2} radians. This suggests a linear relationship to pulse energy, although more calculations are required before completing this assessment. By taking the more realistic situation of using a 100 μm standard deviation beam waist laser, the required $\pi/2$ radians is reached at 8.7 μJ of pulse energy. Importantly, the peak instantaneous fluence attained by this pulse is approximately 2.2 GW/cm^2, similar in fluence to continuous beam ponderomotive phase plates.[31] This is attainable by class 4 pulsed lasers[37] and, at repetition rates of 100 kHz, we hypothesize that 870 mW of power is required to attain the desired phase plate. Higher repetition rates may be required to reach the rapid acquisition rates of modern cryo-EM techniques, although such increases in repetition rate may lead to deleterious effects on the specimen.[43] Nevertheless, the powers required from these simulations closely match in magnitude to the required input powers by other laser-driven phase plates.[31] Indeed, we demonstrate a similar principle by temporally compressing the laser beam while other phase plates rely on resonance cavities to attain high Q factors in the intersection between electron and photon optical axes.[22,32]

It must be noted that while the results of the quasi-classical model match those of the fundamental scattering model, the
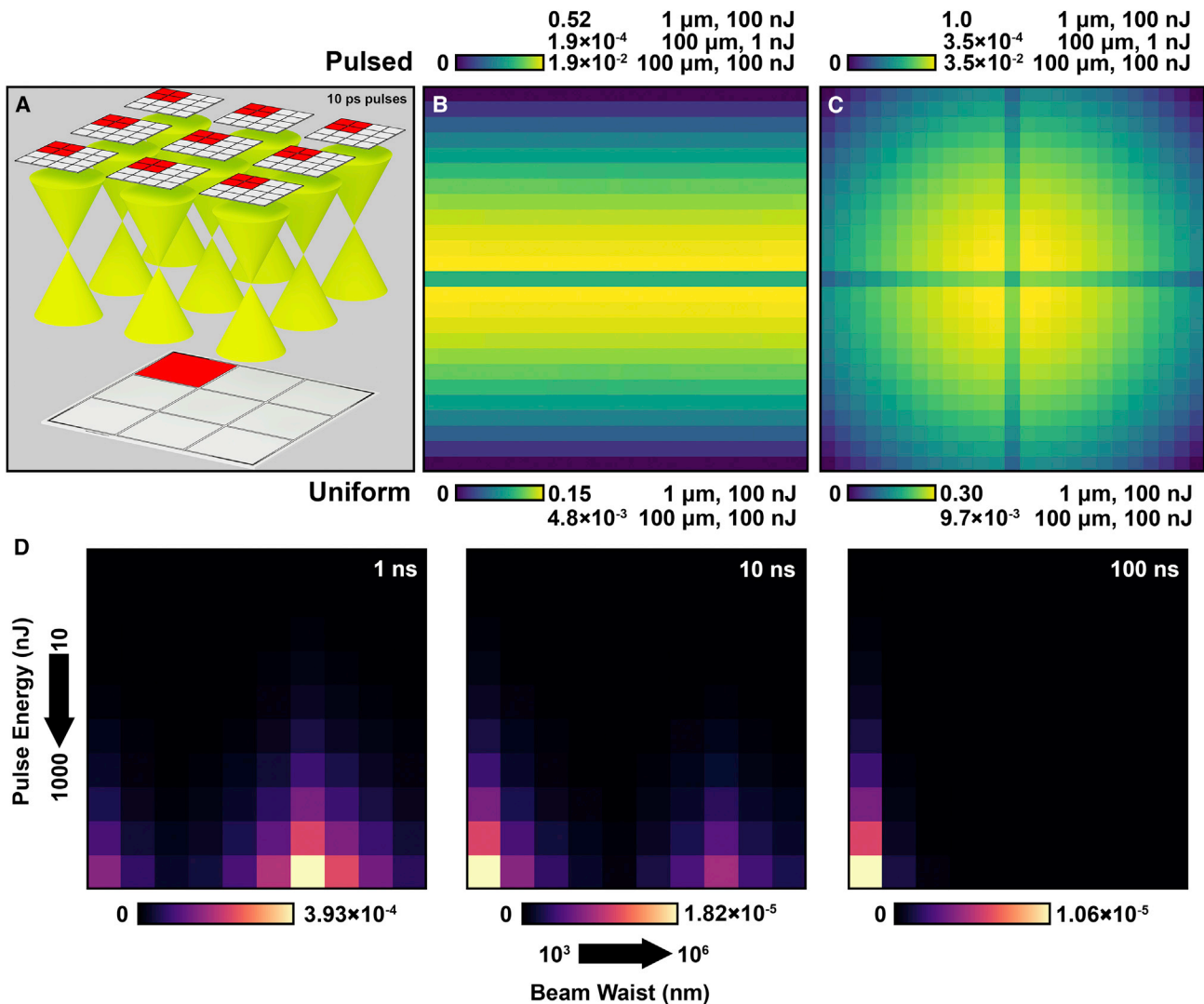
Figure 4. Demonstration of accounting for the finite size of the direct electron beam

(A) Simulation technique used to account for this non-infinitesimally small crossover at specific laser parameters.

(B) Corresponds with solutions to the fundamental scattering model with a single laser while (C) incorporates a second laser. Color bars (units in radians) are included to quantify the resulting phase shift to three separate laser beam parameters, with the pulsed electron emission solutions at the top and the uniform electron emission solutions at the bottom. All results shown in (B and C) were simulated at 10 ps of interaction time.

(D) Exploration of the interaction between a uniform (i.e., stochastically emitted) electron beam and pulsed laser beams. Similar to Figure 2, the peak shifts have been displayed in contour plots as functions of interaction time, pulse energy, and beam waist. These simulations used the infinitesimally small approximation.

simulation itself is greatly restricted by the number of points and mesh size in the *xz*-direction. Ultimately, at a cross-over size of 200 μm, there should be at minimum 400 points to match the wavelength of the photons used in the simulations. However, computational limits greatly hinder this type of calculation and, in this case, only 25 calculation points along each axis were used. Using a diminished number of points leads to aliasing and a shape that is not truly representative of the solution, as demonstrated by the anomalous dip in phase shift at the center of each contour plot. Nonetheless, a brief study in increasing the mesh sizes demonstrates that, while the number of points is unsatisfactory, the resulting shapes are sufficiently close enough to the non-aliased solution.

DISCUSSION

Stochastic versus pulsed electron emission
Before the implementation of pulsed electron beams, it is important to verify whether a strong enough ponderomotive effect is possible in a continuous electron beam. While pulsed beams are compelling for the level of control in emission timing, the deleterious effects from bunching charges are well known.[44] Even in the single-electron regime, variations in hardware at the cathode can greatly affect the emission behavior of electrons and introduce aberrations.[36] As a result, the most ideal condition for the ponderomotive force to occur would be in the native unmodified electron beam. Of course, while the emission of

electrons is largely stochastic in nature when not under ultrafast conditions, the beam can be considered as continuous over longer acquisition times.[43,45–47]

We simulate such a beam by flattening the probability weights of each slice such that any electron has an equal probability of appearing in each slice. The results of this uniform electron emission, presented in Figure 4D, can then be appropriately adjusted to account for the percentage of time that there is no ponderomotive force in the column:

$$\varphi_{average} \approx (2\sigma_t \cdot R) \cdot \varphi_{simulation},$$

where R is the repetition rate of the laser and $\varphi_{simulation}$ is the phase shift calculated in the duration of the ponderomotive force. Ultimately, the necessity of containing a significant fraction of time largely limits most laser capabilities to the nanosecond range; there are few commercially sold pulsed lasers that operate on the femto- or pico-second timescales while still maintaining the necessary repetition rates for efficient temporal coverage of a uniform electron beam (i.e., 100 GHz for 10% coverage in a picosecond laser and 1 THz for 50% coverage in a 500-fs laser). We limit our analysis to nanosecond lasers operating in the much more reasonable MHz range.

Figure 4D clearly shows the peak phase shifts in the uniform electron beam case before adjustments to the proportion of time the laser is in contact with the electron beam. There is no experimental situation where the electron beam experiences a phase shift by $\pi/2$ between 1 and 100 ns of laser pulse duration. When accounting for the case of a finite electron beam focal point, the phase shifts become even less promising, with peak phase shifts of 0.30 radians at dual beam waist of 1 μm, powers of 100 nJ, and pulse durations of 10 ps. The pulse energies required to attain $\pi/2$ phase contrast rapidly exceeds hundreds of μJ per pulse. At MHz frequencies, such powers become unreasonable.

Conclusion

High-resolution cryo-ET is currently a low-contrast imaging technique, requiring under-focusing to generate phase contrast. The widespread use of phase plates in soft matter imaging to enhance contrast is well established and is addressed in the context of cryo-EM. We have discussed in depth the design of a pulsed ponderomotive phase plate by performing an analysis via two mathematical models. Through these models, we find the required phase shift for efficient phase microscopy is achieved most easily through picosecond-duration interactions because of the temporal localization of power in the ultrafast pulses. At 10 ps of temporal resolution, the required energy per pulse is 8.7 μJ, leading to a peak instantaneous fluence of 2.2 GW/cm^2. Importantly, when extending this analysis to nanoseconds of interaction time, the required power becomes significantly large to the point that it exceeds hundreds of micro-Joules. The results of these simulations further suggest that extending the phase plate to uniform electron emission is prohibitively power expensive with current state-of-the-art lasers because of the high repetition rates required to scatter a significant portion of the electrons.

Limitations of the study

We have not treated the de-coherence generated from the scattering of the electrons in the field and future efforts should address if losses in monochromaticity and spatial coherence are prohibitive to the acquisition of high-resolution images. This study provides a theoretical basis for the design of a pulsed ponderomotive phase plate and future applications will focus on enhancing phase contrast in cryo-ET. Parameters that will need to be optimized in experimental studies are (1) the relationship between the size of the back focal plane and the beam waist of the laser, (2) the fluence of the laser beam to account for other scattering effects (e.g., spontaneous Compton scattering), and (3) the coherence of the electron beam before interacting with the pulsed laser beam.

STAR★METHODS

Detailed methods are provided in the online version of this paper and include the following:

- KEY RESOURCES TABLE
- RESOURCE AVAILABILITY
  - Lead contact
  - Materials availability
  - Data and code availability
- METHOD DETAILS
  - Distribution of calculation points
  - Mesh-sizing
- QUANTIFICATION AND STATISTICAL ANALYSIS

AUTHOR CONTRIBUTIONS

A.W.P.F. and D.X.D. conceived the experiments. D.X.D. wrote the MATLAB code to simulate experiments. A.W.P.F. and D.X.D. prepared the manuscript. A.W.P.F. supervised the project.

DECLARATION OF INTERESTS

The authors declare no competing interests.

INCLUSION AND DIVERSITY

We support inclusive, diverse, and equitable conduct of research.

REFERENCES

1. Saleh, A., Noguchi, Y., Aramayo, R., Ivanova, M.E., Stevens, K.M., Montoya, A., Sunidhi, S., Carranza, N.L., Skwark, M.J., and Speck, C.

(2022). The structural basis of Cdc7-Dbf4 kinase dependent targeting and phosphorylation of the MCM2-7 double hexamer. Nat. Commun. *13*, 2915. https://doi.org/10.1038/s41467-022-30576-1.

2. Vasanthakumar, T., Keon, K.A., Bueler, S.A., Jaskolka, M.C., and Rubinstein, J.L. (2022). Coordinated conformational changes in the V1 complex during V-ATPase reversible dissociation. Nat. Struct. Mol. Biol. *29*, 430–439. https://doi.org/10.1038/s41594-022-00757-z.

3. Yip, K.M., Fischer, N., Paknia, E., Chari, A., and Stark, H. (2020). Atomic-resolution protein structure determination by cryo-EM. Nature *587*, 157–161. https://doi.org/10.1038/s41586-020-2833-4.

4. Yuan, Y., Kong, F., Xu, H., Zhu, A., Yan, N., and Yan, C. (2022). Cryo-EM structure of human glucose transporter GLUT4. Nat. Commun. *13*, 2671. https://doi.org/10.1038/s41467-022-30235-5.

5. Cheng, Y., Grigorieff, N., Penczek, P.A., and Walz, T. (2015). A primer to single-particle cryo-electron microscopy. Cell *161*, 438–449. https://doi.org/10.1016/j.cell.2015.03.050.

6. Frank, J. (2017). Advances in the field of single-particle cryo-electron microscopy over the last decade. Nat. Protoc. *12*, 209–212. https://doi.org/10.1038/nprot.2017.004.

7. Nakane, T., Kotecha, A., Sente, A., McMullan, G., Masiulis, S., Brown, P.M.G.E., Grigoras, I.T., Malinauskaite, L., Malinauskas, T., Miehling, J., et al. (2020). Single-particle cryo-EM at atomic resolution. Nature *587*, 152–156. https://doi.org/10.1038/s41586-020-2829-0.

8. Cheng, Y. (2018). Single-particle cryo-EM;How did it get here and where will it go. Science *361*, 876–880. https://doi.org/10.1126/science.aat4346.

9. Tegunov, D., Xue, L., Dienemann, C., Cramer, P., and Mahamid, J. (2021). Multi-particle cryo-EM refinement with M visualizes ribosome-antibiotic complex at 3.5 Å in cells. Nat. Methods *18*, 186–193. https://doi.org/10.1038/s41592-020-01054-7.

10. Tegunov, D., and Cramer, P. (2019). Real-time cryo-electron microscopy data preprocessing with Warp. Nat. Methods *16*, 1146–1152. https://doi.org/10.1038/s41592-019-0580-y.

11. Martínez, M., Jiménez-Moreno, A., Maluenda, D., Ramírez-Aportela, E., Melero, R., Cuervo, A., Conesa, P., Del Caño, L., Fonseca, Y.C., Sánchez-García, R., et al. (2020). Integration of cryo-EM model building software in scipion. J. Chem. Inf. Model. *60*, 2533–2540. https://doi.org/10.1021/acs.jcim.9b01032.

12. Zheng, S.Q., Palovcak, E., Armache, J.-P., Verba, K.A., Cheng, Y., and Agard, D.A. (2017). MotionCor2: anisotropic correction of beam-induced motion for improved cryo-electron microscopy. Nat. Methods *14*, 331–332. https://doi.org/10.1038/nmeth.4193.

13. Himes, B.A., and Zhang, P. (2018). emClarity: software for high-resolution cryo-electron tomography and subtomogram averaging. Nat. Methods *15*, 955–961. https://doi.org/10.1038/s41592-018-0167-z.

14. Stabrin, M., Schoenfeld, F., Wagner, T., Pospich, S., Gatsogiannis, C., and Raunser, S. (2020). TranSPHIRE: automated and feedback-optimized on-the-fly processing for cryo-EM. Nat. Commun. *11*, 5716. https://doi.org/10.1038/s41467-020-19513-2.

15. Punjani, A., Rubinstein, J.L., Fleet, D.J., and Brubaker, M.A. (2017). cryoSPARC: algorithms for rapid unsupervised cryo-EM structure determination. Nat. Methods *14*, 290–296. https://doi.org/10.1038/nmeth.4169.

16. Borsali, R., and Pecora, R. (2008). Soft-matter Characterization (Springer Science & Business Media).

17. Franken, L.E., Boekema, E.J., and Stuart, M.C.A. (2017). Transmission electron microscopy as a tool for the characterization of soft materials: application and interpretation. Adv. Sci. *4*, 1600476. https://doi.org/10.1002/advs.201600476.

18. Porter, K.R., Claude, A., and Fullam, E.F. (1945). A study of tissue culture cells by electron microscopy: methods and preliminary observations. J. Exp. Med. *81*, 233–246. https://doi.org/10.1084/jem.81.3.233.

19. Zernike, F. (1955). How I discovered phase contrast. Science *121*, 345–349.

20. Danev, R., and Nagayama, K. (2001). Transmission electron microscopy with Zernike phase plate. Ultramicroscopy *88*, 243–252. https://doi.org/10.1016/S0304-3991(01)00088-2.

21. Danev, R., Buijsse, B., Khoshouei, M., Plitzko, J.M., and Baumeister, W. (2014). Volta potential phase plate for in-focus phase contrast transmission electron microscopy. Proc. Natl. Acad. Sci. USA *111*, 15635–15640. https://doi.org/10.1073/pnas.1418377111.

22. Müller, H., Jin, J., Danev, R., Spence, J., Padmore, H., and Glaeser, R.M. (2010). Design of an electron microscope phase plate using a focused continuous-wave laser. New J. Phys. *12*, 073011. https://doi.org/10.1088/1367-2630/12/7/073011.

23. Glaeser, R.M. (2013). Invited Review Article: methods for imaging weak-phase objects in electron microscopy. Rev. Sci. Instrum. *84*, 111101. https://doi.org/10.1063/1.4830355.

24. Marko, M., Meng, X., Hsieh, C., Roussie, J., and Striemer, C. (2013). Methods for testing Zernike phase plates and a report on silicon-based phase plates with reduced charging and improved ageing characteristics. J. Struct. Biol. *184*, 237–244. https://doi.org/10.1016/j.jsb.2013.08.008.

25. Danev, R., and Baumeister, W. (2016). Cryo-EM single particle analysis with the Volta phase plate. Elife *5*, e13046. https://doi.org/10.7554/eLife.13046.

26. Pretzsch, R., Dries, M., Hettler, S., Spiecker, M., Obermair, M., and Gerthsen, D. (2019). Investigation of hole-free phase plate performance in transmission electron microscopy under different operation conditions by experiments and simulations. Adv. Struct. Chem. Imag. *5*, 5. https://doi.org/10.1186/s40679-019-0067-z.

27. Wang, H.-W., and Fan, X. (2019). Challenges and opportunities in cryo-EM with phase plate. Curr. Opin. Struct. Biol. *58*, 175–182. https://doi.org/10.1016/j.sbi.2019.06.013.

28. Dries, M., Obermair, M., Hettler, S., Hermann, P., Seemann, K., Seifried, F., Ulrich, S., Fischer, R., and Gerthsen, D. (2018). Oxide-free aC/Zr0.65Al0.075Cu0.275/aC phase plates for transmission electron microscopy. Ultramicroscopy *189*, 39–45. https://doi.org/10.1016/j.ultramic.2018.03.003.

29. Rosi, P., Gazzadi, G.C., Frabboni, S., Grillo, V., Tavabi, A.H., Dunin-Borkowski, R.E., and Pozzi, G. (2021). Focused ion beam fabrication of Janus bimetallic cylinders acting as drift tube Zernike phase plates for electron microscopy. J. Appl. Phys. *130*, 024507. https://doi.org/10.1063/5.0050055.

30. Reed, B.W. (2012). Ponderomotive phase plate for transmission electron microscopes (Google Patents).

31. Turnbaugh, C., Axelrod, J.J., Campbell, S.L., Dioquino, J.Y., Petrov, P.N., Remis, J., Schwartz, O., Yu, Z., Cheng, Y., Glaeser, R.M., and Mueller, H. (2021). High-power near-concentric Fabry–Perot cavity for phase contrast electron microscopy. Rev. Sci. Instrum. *92*, 053005. https://doi.org/10.1063/5.0045496.

32. Henke, J.W., Raja, A.S., Feist, A., Huang, G., Arend, G., Yang, Y., Kappert, F.J., Wang, R.N., Möller, M., Pan, J., et al. (2021). Integrated photonics enables continuous-beam electron phase modulation. Nature *600*, 653–658. https://doi.org/10.1038/s41586-021-04197-5.

33. García de Abajo, F.J., and Konečná, A. (2021). Optical modulation of electron beams in free space. Phys. Rev. Lett. *126*, 123901. https://doi.org/10.1103/PhysRevLett.126.123901.

34. Park, S.T., Lin, M., and Zewail, A.H. (2010). Photon-induced near-field electron microscopy (PINEM): theoretical and experimental. New J. Phys. *12*, 123028. https://doi.org/10.1088/1367-2630/12/12/123028.

35. Byskov-Nielsen, J., Savolainen, J.-M., Christensen, M.S., and Balling, P. (2010). Ultra-short pulse laser ablation of metals: threshold fluence, incubation coefficient and ablation rates. Appl. Phys. A *101*, 97–101. https://doi.org/10.1007/s00339-010-5766-1.

36. Curtis, W.A., and Flannigan, D.J. (2021). Toward Å-fs-meV resolution in electron microscopy: systematic simulation of the temporal spread of

single-electron packets. Phys. Chem. Chem. Phys. *23*, 23544–23553. https://doi.org/10.1039/D1CP03518E.

37. Fitzpatrick, A.W.P., Lorenz, U.J., Vanacore, G.M., and Zewail, A.H. (2013). 4D cryo-electron microscopy of proteins. J. Am. Chem. Soc. *135*, 19123–19126. https://doi.org/10.1021/ja4115055.

38. van Leeuwen, K., Schaap, W., Buijsse, B., Borelli, S., Kempers, S., Verhoeven, W., and Luiten, O. (2022). Feasibility of a pulsed ponderomotive phase plate for electron beams. Preprint at arXiv. https://doi.org/10.48550/arXiv.2209.03201.

39. Yariv, A., and Yeh, P. (2007). Photonics: Optical Electronics in Modern Communications (Oxford University Press).

40. Zhu, J., Penczek, P.A., Schröder, R., and Frank, J. (1997). Three-dimensional reconstruction with contrast transfer function correction from energy-filtered cryoelectron micrographs: procedure and application to the 70SEscherichia coliRibosome. J. Struct. Biol. *118*, 197–219. https://doi.org/10.1006/jsbi.1997.3845.

41. Schwartz, O., Axelrod, J.J., Campbell, S.L., Turnbaugh, C., Glaeser, R.M., and Müller, H. (2019). Laser phase plate for transmission electron microscopy. Nat. Methods *16*, 1016–1020. https://doi.org/10.1038/s41592-019-0552-2.

42. Axelrod, J.J., Campbell, S.L., Schwartz, O., Turnbaugh, C., Glaeser, R.M., and Müller, H. (2020). Observation of the relativistic reversal of the ponderomotive potential. Phys. Rev. Lett. *124*, 174801. https://doi.org/10.1103/PhysRevLett.124.174801.

43. VandenBussche, E.J., and Flannigan, D.J. (2019). Reducing radiation damage in soft matter with femtosecond-timed single-electron packets. Nano Lett. *19*, 6687–6694. https://doi.org/10.1021/acs.nanolett.9b03074.

44. VandenBussche, E.J., Clark, C.P., Holmes, R.J., and Flannigan, D.J. (2020). Mitigating damage to hybrid perovskites using pulsed-beam TEM. ACS Omega *5*, 31867–31871. https://doi.org/10.1021/acsomega.0c04711.

45. Nijkerk, M.D., and Kruit, P. (2004). Stochastic Coulomb interactions in space charge limited electron emission. J. Appl. Phys. *96*, 2985–2989. https://doi.org/10.1063/1.1777395.

46. Kruit, P. (2020). Cathodes for electron microscopy and lithography. In Modern Developments in Vacuum Electron Sources, G. Gaertner, W. Knapp, and R.G. Forbes, eds. (Springer International Publishing), pp. 251–292. https://doi.org/10.1007/978-3-030-47291-7_6.

47. Bücker, K., Picher, M., Crégut, O., LaGrange, T., Reed, B.W., Park, S.T., Masiel, D.J., and Banhart, F. (2016). Electron beam dynamics in an ultrafast transmission electron microscope with Wehnelt electrode. Ultramicroscopy *171*, 8–18. https://doi.org/10.1016/j.ultramic.2016.08.014.

STAR★METHODS

KEY RESOURCES TABLE

REAGENT or RESOURCE	SOURCE	IDENTIFIER
Software and algorithms		
As described in the main text and found on GitHub in the provided links.	github.com/FitzpatrickLab/PPPP	https://doi.org/10.5281/zenodo.7365610

RESOURCE AVAILABILITY

Lead contact
Further information and requests for resources should be directed to Anthony Fitzpatrick (anthony.fitzpatrick@columbia.edu).

Materials availability
This study did not generate unique reagents.

Data and code availability
- All data reported in this paper will be shared by the lead contact upon request.
- All original code has been deposited at github.com/DuXDaniel/PPPP and at github.com/FitzpatrickLab/PPPP which are publicly available. DOIs are listed in the key resources table.
- Any additional information reported in this paper is available from the lead contact upon request.

METHOD DETAILS

As described previously, these models were adapted from previously published literature describing the phase shift in Compton scattering and fit to a forward-stepping algorithm to determine the influence of ultrafast pulses on the phenomenon.[22,31] More specifically, the electron beam is split into slices and each slice is individually stepped through time as it passes through the laser beam, beginning three laser pulse spatiotemporal radii (3σ, 99.7%) away from the center of the intersection region. The crossover slope for the electrons is set to be over the span of a foot (300 mm). At the end of each slice calculation, it is averaged into the total amount of slices that form the full electron pulse. Numerous concessions were made to improve simulation times, including the ignoring of electron beam diameter at the crossover point (d_{xo}) and a loss in granularity of the forward-stepping algorithm (121 side-length voxel cube). It is important to note that this pinched crossover artificially increases the phase shift of the electrons and is the cause for the section dedicated to size effects in both models. Finally, we assume a non-interaction regime between electrons.

Distribution of calculation points
The simplest form of distributing calculation points in the mesh of a finite element model (FEM) is an even spread across time and space, agnostic to the geometry of the specimen or form of excitation to the system. However, this can lead to results that are poorly representative of the true solution. To curb any skewing of the data, a weighted distribution of points is often generated that concentrates more calculation points toward regions of the system where interactions are more likely to occur.

In the context of the pulsed ponderomotive phase plate, the regions of interest would be when the photon pulses and electron beam meet and fully overlap. Within the simulation itself, we split the electron beam into the mesh and use a mathematical formulation of the laser beam to calculate the strength of the interactions. As such, the weighted mesh contains the density of electrons within the electron pulses. For the infinitesimally small crossover calculations, the mesh in the xz-plane, or the plane normal to the travel path, is distributed evenly as the incident electron beam is coherent and collimated from the illumination lenses. However, the distribution of points in the y axis is weighted by the method in which the electrons are emitted. For an ultrafast photoexcited pulse, this shape would similarly take the form of a Gaussian.

For a finite crossover, the calculation becomes somewhat more complex. In the previous example, the distribution was assumed to be uniform due to the parallel illumination provided by the electron optics. However, in the case where we observe a finite-sized direct beam in the back-focal-plane, the distribution is closer to a Gaussian or a Lorentzian, depending on the instrument response function. Thus, in the final averaging of phases for electrons traveling at congruent angles, the final value must be weighted by the shape of the contour of the direct beam. In the paper, we mentioned this took the characteristic of a 200 μm aperture.

Mesh-sizing

The size of the mesh is also important. Obviously, a single data point cannot be used as the basis for the calculation. While the ideal number of points is infinity, such large array sizes are unreasonable and simply cannot exist with current memory capabilities. Thus, a series of tests were performed with weighted meshes to discover the ideal mesh size in the x, y, and z directions.

QUANTIFICATION AND STATISTICAL ANALYSIS

The software used in the main text is not based on stochastically-driven algorithms. As such, there is no statistical analysis to perform. The quantification of the data itself follows standard descriptions for resulting values of phase shift in the electrons (*i.e.* radians). While there were a few hardware limitations, these have been thoroughly discussed in the main text (*e.g.* memory caps and CPU clock speeds).